

1 **Alleloscope: Integrative single cell analysis of allele-specific copy**
2 **number alterations and chromatin accessibility in cancer**

3 Chi-Yun Wu^{1,2}, Billy T. Lau^{3,4}, Heonseok Kim³, Anuja Sathe³, Susan M. Grimes⁴, *Hanlee
4 P. Ji^{3,4}, *Nancy R. Zhang^{1,2}

5 **Institutions**

6 ¹Graduate Group in Genomics and Computational Biology, University of Pennsylvania,
7 Philadelphia, PA

8 ²Department of Statistics, University of Pennsylvania, Philadelphia, PA

9 ³Division of Oncology, Department of Medicine, Stanford University School of Medicine,
10 Stanford, CA

11 ⁴Stanford Genome Technology Center, Stanford University, Palo Alto, CA

12 *Corresponding author

13 **Corresponding authors**

14 Hanlee P. Ji

15 Email: genomics_ji@stanford.edu

16 Nancy R. Zhang

17 Email: nzh@wharton.upenn.edu

18

19 **Abstract**

20 Cancer progression is driven by both somatic copy number aberrations (CNAs) and
21 chromatin remodeling, yet little is known about the interplay between these two classes
22 of events in shaping the clonal diversity of cancers. We present Alleloscope, a method
23 for allele-specific copy number estimation that can be applied to single cell DNA and
24 ATAC sequencing data, either separately or in combination. This approach allows for
25 integrative multi-omic analysis of allele-specific copy number and chromatin accessibility
26 on the same cell. On scDNA-seq data from gastric, colorectal, and breast cancer samples,
27 with extensive validation using matched linked-read sequencing, Alleloscope finds
28 pervasive occurrence of highly complex, multi-allelic copy number aberrations, where
29 cells that carry varying allelic configurations adding to the same total copy number co-
30 evolve within a tumor. The contributions of such allele-specific events to intratumor
31 heterogeneity have been under-reported and under-studied due to the lack of methods
32 for their detection. On scATAC-seq from two basal cell carcinoma samples and a gastric
33 cancer cell line, Alleloscope detects multi-allelic copy number events and copy neutral
34 loss-of-heterozygosity, enabling the dissection of the contributions of chromosomal
35 instability and chromatin remodeling in tumor evolution.

36 **Introduction**

37 Cancer is a disease caused by genetic alterations and epigenetic modifications
38 which, in combination, shape the dysregulated transcriptional programming of tumor
39 cells^{1, 2}. These somatic genomic events lead to a diverse cellular population from which
40 clones with advantageous alterations proliferate and eventually metastasize³. The
41 comprehensive study of cancer requires the integrative profiling of genetic and epigenetic
42 changes at the resolution of single cells. We combined the analysis of two such genomic
43 dimensions – DNA copy number and chromatin accessibility – through massively parallel
44 single cell sequencing assays.

45 First, consider copy number aberrations (CNAs), through which we have derived much of
46 our current understanding of the relationship between genome instability and tumor
47 evolution⁴. Total copy number profiling, which estimates the sum of the copy numbers of
48 the two homologous chromosomes, is inadequate to characterize some types of cancer
49 genomic aberrations. Such events include the pervasively occurring copy-neutral loss of
50 heterozygosity (LOH)⁵⁻⁸, intriguing “mirrored events”^{9, 10} where a given tumor may have
51 cancer cells carrying amplification of one haplotype are intermingled with cancer cells
52 carrying amplification of the other haplotype, and the even more complex alterations that
53 are only detectable through allele-specific analysis¹¹. While the importance of allele-
54 specific copy number has been emphasized in bulk DNA sequencing analysis^{5-8, 11}, most
55 single-cell CNV analysis considers only total copy number due to low per-cell coverage¹²⁻
56 ¹⁹. Recently, Zaccaria et al. developed CHISEL¹⁰, a method for single-cell allele-specific
57 copy number analysis, but requires externally phased haplotypes based on large

58 reference cohorts. Despite these advances, there remain many missing details about the
59 genomic landscape of allelic imbalances when considering single cells.

60 Epigenetic modifications are also an important genomic feature of cancer. Analysis of
61 chromatin structure is feasible with a variety of methods including transposase-accessible
62 chromatin sequencing (ATAC-seq). This approach is applied either with conventional
63 bulk-based or single-cell sequencing. Subsequently, analysis of chromatin structure has
64 shown that epigenetic remodeling modulates the plasticity of cells in cancer²⁰⁻²⁴, leads to
65 stem-like properties²⁵⁻²⁷ and generates therapeutic resistance²⁸⁻³¹. Since copy number
66 alterations involve large gains and losses of available chromatin, we expect the chromatin
67 accessibility of a region to be influenced by the changes in underlying copy number.
68 Current scATAC-seq studies estimate total copy number profiles by smoothing the read
69 coverage and normalizing the signals against a control cell population, yet this
70 appropriate control is often difficult to identify^{23,32}. Currently, there is no method for reliable
71 total or allele-specific copy number profiling in scATAC-seq data, and thus, how to
72 disentangle the effects of CNA and chromatin remodeling in shaping the epigenetic
73 landscape remains a challenge.

74 Addressing these challenges, we present Alleloscope, a method for **allele-specific copy**
75 **number estimation** and multiomic profiling in single cells. Alleloscope does not rely on
76 external phasing information, and can be applied to scDNA-seq data or to scATAC-seq
77 data with sample-matched bulk DNA sequencing data. To interrogate the single cell
78 landscape of allele-specific CNA, we first apply Alleloscope on scDNAseq data from four
79 gastric cancer samples, four colorectal cancer samples, and a breast cancer sample^{10, 12,}
80 ³³. For three of the gastrointestinal cancer samples, results are extensively validated by

81 10x linked-read sequencing which provides accurate phasing information³⁴⁻³⁶. In these
82 datasets, Alleloscope accurately identifies LOH and mirrored-subclonal amplification
83 events, and finds pervasive occurrence of highly complex, multi-allelic loci, where cells
84 that carry varying allelic configurations adding to the same total copy number co-evolve
85 within a tumor. The ubiquity of such events in all three cancer types analyzed reveal that
86 they may be an important overlooked source of intratumor genetic heterogeneity.

87 Having characterized the complexity of allele-specific CNA events at single cell resolution,
88 we turn to scATAC-seq data from two basal cell carcinoma samples with paired bulk
89 whole exome sequencing data²³ and a complex polyclonal gastric cancer cell line that we
90 analyzed by scDNA-seq. In these samples, we evaluate the accuracy of Alleloscope in
91 genotyping and clone assignment and demonstrate its application to the integrative
92 analysis of CNA and chromatin accessibility.

93 **Results**

94 **Overview of Alleloscope allele-specific copy number estimation**

95 First, we briefly overview Alleloscope's method for allele-specific copy number estimation
96 (Figure 1). Clone assignment and integration with peak signals in scATAC-seq data will
97 be described later. Alleloscope relies on two types of data features: coverage, derived
98 from all reads that map to a given region, and allelic imbalance, derived from allele-
99 informative reads that cover heterozygous loci in the region. We start with some essential
100 definitions. For a given single nucleotide polymorphism (SNP) site, we refer to its mean
101 coverage across cells as *bulk coverage* and its mean variant allele frequency (VAF = ratio
102 of alternative allele read count to total read count) across cells as its *bulk VAF*. Between

103 the two parental haplotypes, we define the term “major haplotype” as the haplotype with
104 higher mean count across cells. Note that a haplotype may be the “major haplotype” of a
105 sample, but be the haplotype with lesser copy number within some cells. For each
106 individual cell i , in any given CNA region, we define two key parameters: (1) the major
107 haplotype proportion (θ_i), defined as the count of the major haplotype divided by the total
108 copy number for the region, and (2) total copy fold change (ρ_i), defined as the ratio of the
109 total copy number of the region in the given cell relative to that in normal cells.

110 The genotyping algorithm starts by segmenting the genome into regions of homogeneous
111 allele-specific copy number using both the bulk coverage and bulk VAF profiles (Fig.1
112 Step 2). This can be achieved by multiple existing algorithms, which may be combined to
113 increase detection sensitivity, see Methods for details. In our analyses of scATAC-seq
114 data, the segmentation relied on the matched scDNA-seq data or the whole-exome
115 sequencing data, which ensures that the putative CNA regions considered for genotyping
116 are not confounded by the broad chromatin remodeling that occur in cancer.

117 Now consider each putative CNA region. An expectation-maximization (EM) based
118 algorithm is used to iteratively phase each SNP and estimate the major haplotype
119 proportion (θ_i) for each cell (Fig. 1, step 3). For each SNP j , let $I_j \in \{0,1\}$ be the indicator
120 of whether the reference allele of SNP j is a component of the major haplotype. An initial
121 estimate $\hat{I}_j^{(0)}$ is first derived from the bulk VAF profile. Then, in iteration t , Alleloscope
122 computes $\hat{\theta}_i^{(t)}$ by pooling counts across sites within the region, weighted by the current
123 phasing $\hat{I}_j^{(t)}$, then updates the estimate of I_j based on $\hat{\theta}_i^{(t)}$ by pooling counts across cells.
124 The estimates of θ_i and I_j usually converge within a few iterations as described in the

125 Methods. If matched scDNA-seq data are available for a sample sequenced by scATAC-
126 seq, I_j values can be estimated from scDNA-seq and then used to compute θ_i for each
127 cell in the scATAC-seq data, enabling integration of the two data types.

128 The estimated major haplotype proportions ($\hat{\theta}_i$'s), along with a preliminarily normalized
129 coverage statistic ($\tilde{\rho}_i$), are then used to identify a set of normal cells and diploid regions
130 (Fig. 1, Step 4). This information is used to estimate an improved relative coverage fold-
131 change ($\hat{\rho}_i$) for each cell within each CNA region. If cell i 's true allele-specific copy
132 numbers are homogeneous within the given region, then its true value of (θ_i, ρ_i) should
133 belong to a set of canonical points displayed in Step 5 of Figure 1. Thus, the estimated
134 values $(\hat{\rho}_i, \hat{\theta}_i)$ are clustered across cells and associated with one of the canonical values
135 to yield the cell-level haplotype profiles for the CNV region. These cell- and region-specific
136 haplotype profiles serve as the base for clone assignment and subsequent integration
137 with peak signals in scATAC-seq data. (Fig. 4b).

Figure 1.

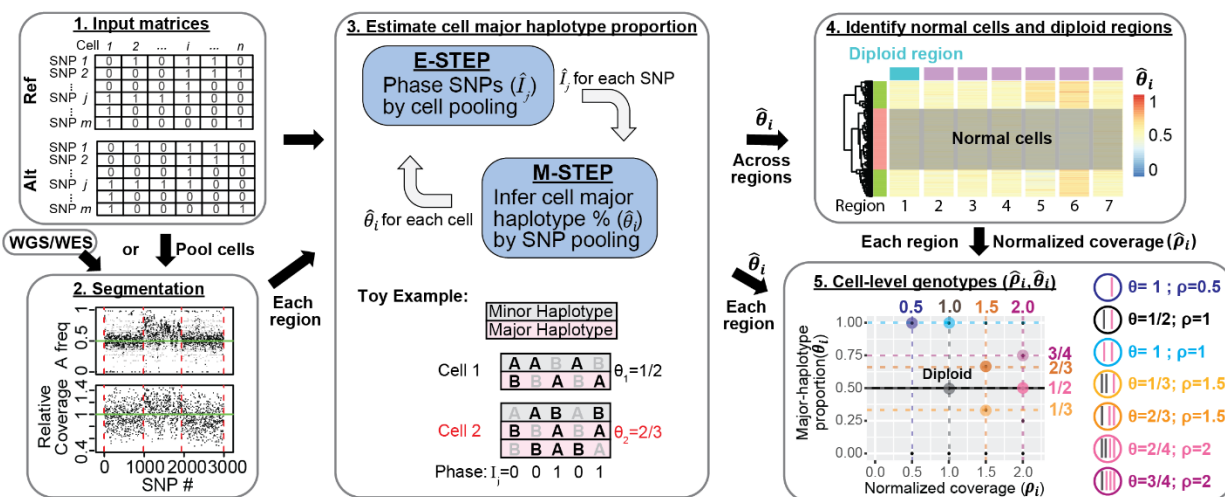


Fig. 1: Overview of allele-specific copy number estimation of single cells with Alleloscope. 1. The algorithm operates on raw read count matrices for reference allele (Ref) and alternative allele (Alt) computed from single cell DNA or ATAC sequencing. 2. First, we obtain a segmentation of the genome based on sample-matched whole genome or whole exome sequencing data using FALCON⁵. If scDNA-seq is available, cells can be pooled to derive a pseudo-bulk. 3. For each region derived from the segmentation, simultaneously phase SNPs (\hat{I}_j) and estimate cell major haplotype proportion ($\hat{\theta}_i$) by expectation maximization (EM) algorithm. Since we are focusing on only one region, the region indicator is suppressed in our notation here. In the E-step, information is pooled across cells to estimate the phasing of each SNP. In the M-step, information is pooled across all SNPs in the region are pooled to estimate the major haplotype proportion $\hat{\theta}_i$ for each cell. The toy example shows a scenario with two cells for a region containing 5 SNPs, with cell 2 carrying an amplification of the major haplotype (in pink). For each cell and each SNP, alleles that are observed in a sequenced read are bolded in black (we assume that only one read is observed, reflecting the sparsity of the data). The true phase (I_j) of the SNPs and the true major haplotype proportion ($\hat{\theta}_i$) are shown. 4. For region r let $\{\hat{\theta}_{ir}\}$ be its estimated major haplotype proportions across cells i . Pool data across regions to identify candidate normal cells and candidate normal regions for computing a normalized coverage $\hat{\rho}_{ir}$ for region r in cell i . 5. Alleloscope assigns integer allele-specific copy numbers to each cell for each region based on the ($\hat{\rho}_{ir}, \hat{\theta}_{ir}$) pairs.

139 **Whole genome haplotypes validate Alleloscope in scDNA-seq allele-specific copy**
140 **number estimation**

141 First, we explore the single cell landscape of allele-specific CNAs using scDNA-seq data.
142 To validate the phasing and genotyping accuracy of Alleloscope in scDNA-seq data, we
143 used matched linked-read whole-genome sequencing data on three gastrointestinal
144 tumor samples: P5931, P6335 and P6198. Linked-read sequencing, in which one derives
145 reads from individual high molecular weight DNA molecules, provides variants that can
146 be phased into extended haplotypes covering Mb³⁴⁻³⁶. As a result, one obtains accurate,
147 Mb-scale haplotype information from cancer genome. To evaluate the accuracy of
148 phasing, we compared the haplotypes estimated by Alleloscope to the haplotypes
149 obtained from linked-read WGS. Additionally, we used the WGS haplotype to evaluate
150 the allele-specific copy number estimation for each cell and to assess the impact of
151 phasing errors on genotyping accuracy (Fig. 2a).

152 Figure 2b shows the results for the gastric cancer sample from P5931, whose genome-
153 wide copy number profile indicates clear CNA events on four chromosomes—chr7, chr8,
154 chr20, and chr21. For each event, the scatter plots of $(\hat{\theta}_i, \hat{\rho}_i)$ estimated by Alleloscope
155 and colored by haplotype profiles, are shown in Fig. 2c. Note that the $(\hat{\theta}_i, \hat{\rho}_i)$ clusters fall
156 almost directly on top of the expected canonical values (e.g. (1/2, 1) for diploid, (2/3, 1.5)
157 for 1 copy gain of major haplotype). Interestingly, chromosomes 7, 8, and 21 each show
158 subclonal clusters have differing allelic ratios but the same total copy number, which
159 would not be detectable without allele-specific estimation. We denote the major haplotype
160 of a region by “M”, and the minor haplotype by “m”. The chromosome 7 amplification

161 exhibits two tumor subclones with mirrored-subclonal CNAs (MMm and Mmm), each
162 subclone amplifying a different haplotype. Such a mirrored-subclonal CNA configuration
163 is also observed for the deletion on chromosome 21 (M- and m-). The chromosome 8
164 amplification exhibits as four tumor subclones with different haplotype profiles— MMm,
165 Mmm, MMmm, and MMMm.

166 We compared the phasing estimated by Alleloscope (\hat{I}_j) against the whole genome
167 haplotypes. The phasing accuracy is 98% for the deleted region (chr21), ~90% for the
168 two clonal amplifications (on chr8 and chr20), and 79% for the subclonal chr7
169 amplification (shown in the titles of the scatter plots of Fig. 2c). Moreover, we evaluated
170 the genotyping accuracy for some of the somatic alterations. Figure 2d shows scatterplots
171 of \hat{p}_i against major haplotype proportion computed using haplotypes derived from linked-
172 read sequencing ($\tilde{\theta}_i$), with the same coloring as Figure 2c. Comparing the scatterplots in
173 Figure 2d to their counterparts in Figure 2c reveals that Alleloscope's estimated cell
174 haplotype profiles are highly concordant with those derived directly with the haplotypes
175 from linked-read WGS. Specifically, the concordance is ~100% across all four events (the
176 concordance for each event is labeled in the scatter plots of Figure 2d). This shows that
177 the genotyping algorithm in Alleloscope is robust to errors in phasing (e.g. for chr7).
178 Similar analysis performed for P6335 is given in Supplementary Fig. 1. We also applied
179 CHISEL on P5931, yet it did not work well for this sample due to the low coverage
180 (Supplementary Fig. 2).

Figure 2.

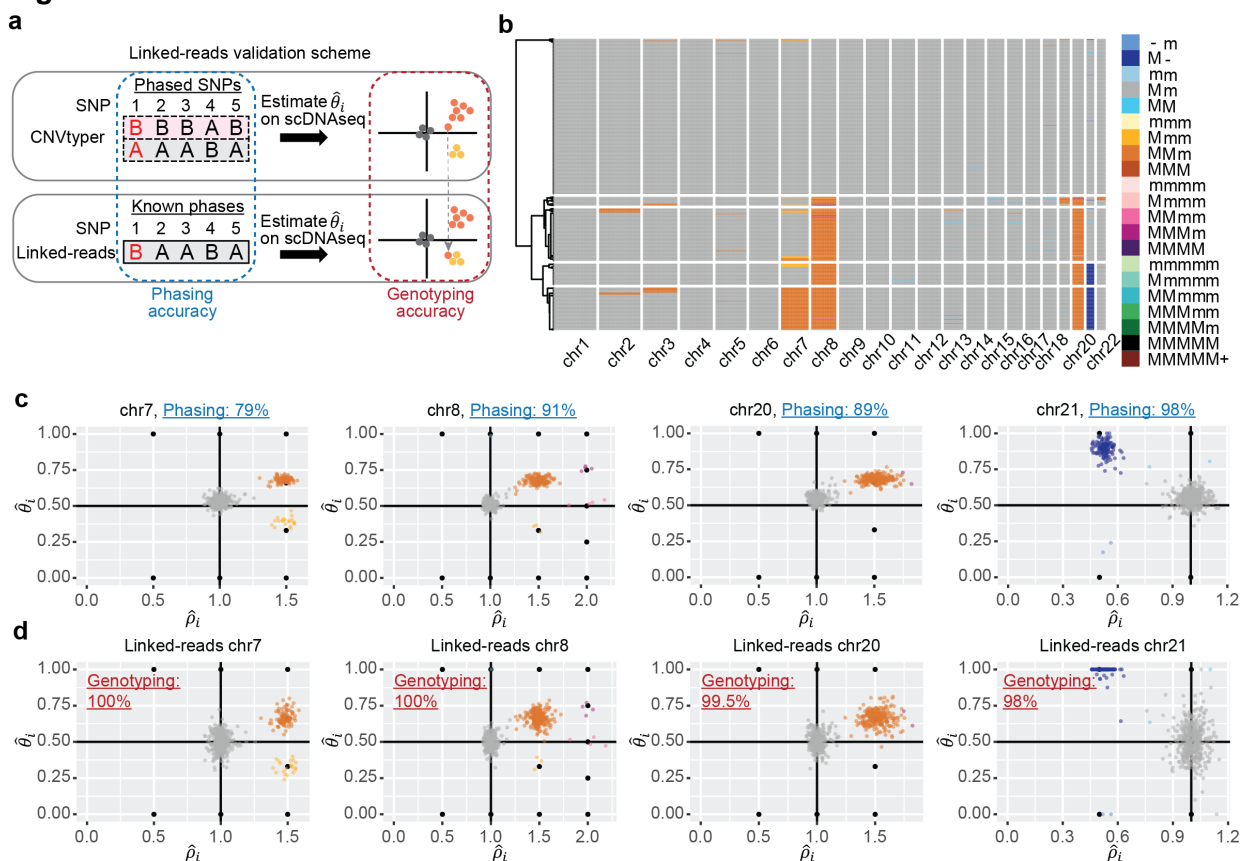


Fig. 2: Validation of the Alleloscope results on the P5931 gastric cancer patient sample and linked-reads sequencing data. (a) Illustration of the validation scheme using linked-reads sequencing data. Phasing accuracy and genotyping accuracy are used to assess performance of the method. (b) Hierarchical clustering of cells in the P5931t sample based on allele-specific copy numbers given by Alleloscope, showing normal cells and 4 main clones, as well as a number of small clones marked by highly confident low-frequency mutations. M: Major haplotype, m: minor haplotype. (c) $(\hat{\rho}_{ri}, \hat{\theta}_{ri})$ estimated by Alleloscope for four regions, colored by the inferred haplotype profile. Note that clusters fall on canonical points corresponding to discrete allele-specific copy number configurations. Phasing accuracy for each region is shown in the plot title. In the color legend, M and m represent the “Major haplotype” and “minor haplotype” respectively. (d) Similar to (c), with $\hat{\theta}_i$ estimated using known SNP phases from matched linked-reads sequencing data, colored by the haplotype profiles assigned in (c) using Alleloscope without the given phasing information. Genotyping accuracy is labeled in the plots.

182 Since copy neutral LOH events, common in cancer genomes, can only be identified
183 through allele-specific copy number analysis. We examined the accuracy of Alleloscope
184 specifically for copy-neutral LOH events with a colorectal adenocarcinoma from P6198.
185 This tumor sample had a conventional WGS profile revealing several copy-neutral LOH
186 regions that were not evident when considering the copy number heatmap in cellranger
187 (Fig. 3a). Chromosome 5 presents an illustrative example: The bulk VAF clearly
188 separates this chromosome into two main regions, a normal region followed by a copy-
189 neutral LOH (Fig. 3b). Concordantly, Alleloscope reveals a cluster centered at $(\rho, \theta) =$
190 $(1,1)$ corresponding to copy-neutral LOH only for the region on the right (Fig. 3b), which
191 cleanly separates the tumor cells from normal cells. Comparing to the haplotype profiles
192 derived using the haplotypes from linked-read WGS for this sample showed that the
193 accuracy of Alleloscope for copy-neutral LOH events is nearly 100% (Supplementary Fig.
194 3).

Figure 3.

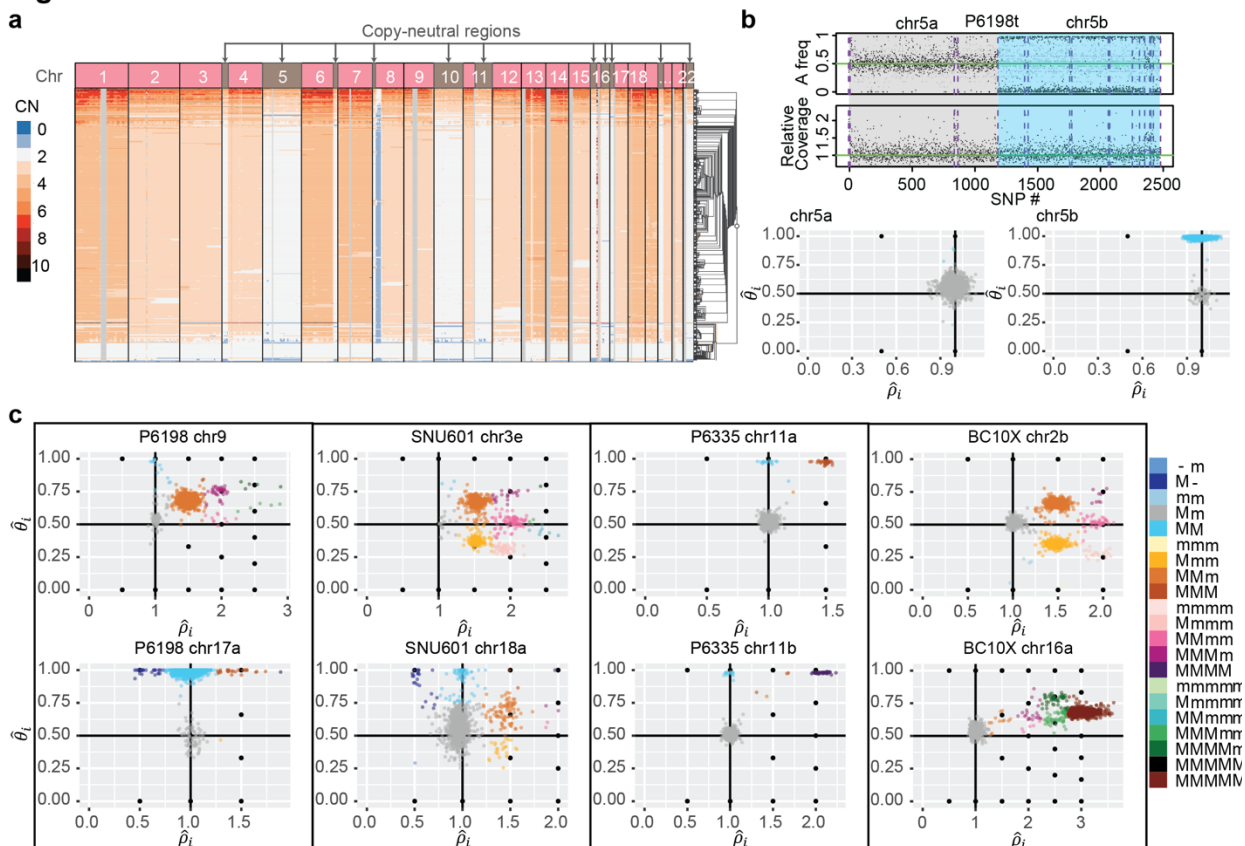


Fig. 3: Across multiple cancer types, Alleloscope detects loss-of-heterozygosity events and multi-allelic copy number aberrations, delineating complex subclonal structure which are invisible to total copy number analysis. (a) The Cell Ranger hierarchical clustering result for P6198t with copy-neutral regions labeled (total 512 cells). (b) Top: FALCON segmentation of P6198t chr5 into two regions with different allele-specific copy number profiles. Bottom: Detailed haplotype profiles of the two regions from Alleloscope, showing that the first region is diploid across cells and the second region has a loss-of-heterozygosity for a subpopulation of cells. The a and b following the chromosome number denote two ordered segments.

(c) Single cell allele-specific estimates ($\hat{\rho}_i$, $\hat{\theta}_i$), colored by assigned haplotype profiles, for select regions in the samples P6198t (metastasized colorectal cancer sample), SNU601 (gastric cancer cell line), P6335 (colorectal cancer sample), and BC10X (breast cancer cell line). In the color legend, M and m represent the “Major haplotype” and “minor haplotype” respectively. The lower-case letters following the chromosome number in the titles denote the ordered genomic segments.

196 **Alleloscope finds pervasive occurrence of polyclonal CNA regions differentiated**
197 **by haplotype ratios**

198 The scDNA-seq samples included in this study are shown in Table 1 of Methods, with
199 detailed segmentation plots and heatmaps for genome-wide allele-specific copy number
200 profiles in supplementary figure 4-10. Across most of the samples, we observed a high
201 prevalence of complex subclonal CNAs indicated by multiple clusters of different
202 haplotype structures within a given genomic region with prototypical examples from
203 P6198, SNU601, P6335 and BC10X shown in Figure 3c. In some regions, such as
204 chromosome 9 of SNU601, 3q of SNU601, 2q and 16p of BC210x, we see as many as
205 seven subclonal clusters for a single event. In many cases there are multiple clusters
206 corresponding to the same total copy number but varying in allelic dosage. Minor
207 subclones carrying deletion of one haplotype can be easily masked by dominant
208 subclones carrying amplifications of the other haplotype in a conventional sequencing
209 analysis without the benefit of single cell resolution or an analysis that considers only
210 copy number without allelic information. Overall, the high subclonal diversity in these
211 genomic regions reveal an aspect of intratumor heterogeneity that was previously
212 undetectable.

213 Recurrent chromosomal instability events, affecting both haplotypes and producing
214 gradients in haplotype dosage, is a common theme across all samples analyzed.
215 Consider, for example, the region on chromosome 9 of P6198, which reveals 7
216 subpopulations of cells: besides the normal cell cluster and the dominant tumor cell
217 cluster with the haplotype profile MMm, there is a small cluster of cells with copy neutral
218 LOH, two small subclones at four chromosome copies and two more at five chromosome

219 copies. This produces major haplotype ratios of $\{\frac{1}{2}, \frac{3}{5}, \frac{2}{3}, \frac{4}{5}, 1\}$ in different cells, possibly
220 conferring different fitness values. Another example of such complexity is chromosome
221 3q of SNU 601 and chromosome 2q of BC10x, which share a similar pattern: two
222 mirrored-subclonal CNAs (MMm, mmM) at total copy number of 3, as well as mirrored-
223 subclonal CNAs (MMMm, MMmm, mMMM) at total copy number of 4, producing a
224 gradient of haplotype ratios $\{\frac{1}{4}, \frac{1}{3}, \frac{1}{2}, \frac{2}{3}, \frac{3}{4}\}$. Interrogating the evolutionary route by which
225 such diversity was achieved, Alleloscope reveals that a whole genome doubling event is
226 highly likely to have taken place early in the development of BC10x and P6198, but not
227 in the development of SNU601 (see Supplementary Fig. 4&6). Thus, the subclones at 2q
228 in BC10x and 3q in SNU601 must have evolved through different evolutionary routes: In
229 BC10x, the early whole-genome doubling produces the cluster MMmm, from which the
230 other clusters of different haplotype profiles were most likely derived through successive
231 loss and gene conversion events. On the contrary, the clusters on 3q of SNU601 were
232 most likely a result of successive amplification events starting from the normal haplotype
233 profile Mm. The fact that different evolutionary routes, in two different cancer types (breast
234 and gastric) evolved to have such similar allelic-specific copy number patterns imply that
235 such haplotype dosage gradients may serve as an important substrate for selection in
236 tumor evolution.

237 Another recurring theme is the co-occurrence of LOH and amplification within the same
238 region. Often, the loss and amplification affect different haplotypes, as for chromosome
239 17p of P6198 and chromosome 11p, 11q of P6335. For 17p of P6198, a gene conversion
240 leading to copy-neutral LOH is most likely the early event, followed by separate loss and
241 gain events that lead to the clusters M- and MMM. Curiously, extreme instability of a

242 chromosome region leads to clones with LOH of a given haplotype coexisting with clones
243 that have the same haplotype amplified. Such clones would have been undetectable in a
244 conventional bulk WGS analysis or even a single cell analysis based solely on total
245 coverage. For example, this is what occurred for SNU601's chr18a (Figure 3c). Using the
246 procedure in Figure 2a, we validated our findings of these multiallelic subclones in P6198
247 and P6335 by comparing to the paired linked-reads sequencing data. Phasing accuracy
248 is high for all LOH and amplification event types that create an allelic imbalance
249 (Supplementary Fig. 3).

250 **Juxtaposition of single cell copy number and chromatin remodeling events by** 251 **integrative scATAC-seq analysis**

252 To illustrate the integrative analysis of scATAC-seq data, we first consider two basal cell
253 carcinoma samples with matched whole-exome sequencing (WES) data³⁷. Using the
254 matched WES data, the genome of each sample was first segmented into regions of
255 homogeneous bulk copy number (Fig. 4a, middle panel shows the segmentation for
256 SU008). Alleloscope was then applied to the scATAC-seq data to derive allele-specific
257 copy number estimates of each cell in each region. Scatterplots of $(\hat{\rho}, \hat{\theta})$ for five example
258 CNA regions and 1 control region (chr12) from SU008 are shown in Fig. 4a. For this
259 sample, peak profiles characterizing chromatin accessibility separated the cells
260 confidently into three main clusters: 308 tumor cells, 259 fibroblasts and 218 endothelial
261 cells. Since normal cells are not expected to carry broad copy number events, we
262 compared the $(\hat{\rho}, \hat{\theta})$ values of the tumor cells against those of the fibroblast and epithelial
263 cells to assess our genotyping accuracy. Density contours for each cell type are shown

264 in the $(\hat{\rho}, \hat{\theta})$ - scatterplots (Fig. 4a). The $(\hat{\rho}, \hat{\theta})$ values clearly separate the tumor cells from
265 the normal cells for each CNV region, with the tumor cell cluster positioned at canonical
266 points, indicating that these statistics used by Alleloscope can accurately distinguish
267 amplifications and loss-of-heterozygosity events in scATAC-seq data. In particular,
268 Alleloscope differentiated the cells that carry copy neutral LOH events through shifts in
269 major haplotype proportion. Note that normal cells, which are not expected to carry broad
270 chromosome-scale CNVs, exhibit chromosome-level deviations in total coverage due to
271 broad chromatin remodeling as exemplified by the chr6b region. Furthermore, many
272 regions with no CNA signal in bulk WES data also exhibit shifts in aggregate coverage in
273 ATAC data, but with no significant difference in their $\hat{\theta}_i$ distribution. Thus, relying solely
274 on shifts in coverage, without complementary shifts in major haplotype proportion, would
275 lead to false positive copy number detections for scATAC-seq data.

276 By assigning allele-specific CNA profiles to single cells in scATAC-seq data, Alleloscope
277 allows the integrative analysis of chromosomal instability and chromatin remodeling as
278 follows (Figure 4b): The scATAC-seq data, paired with bulk or single-cell DNA sequencing
279 data, allows us to detect subclones. In parallel, a peak-by-cell matrix can be computed
280 following standard pipelines. Then, the subclone memberships or CNA profiles can be
281 visualized on the low-dimensional embedding of the peak matrix, and the subclones can
282 be further compared in terms of peak or transcription factor motif enrichment. Precise
283 haplotype profiles for each subclone then allow us to identify significantly
284 enriched/depleted peaks after accounting for copy number differences, thus delineating
285 events that are uniquely attributable to chromatin remodeling.

286 Hierarchical clustering using major haplotype proportion $\hat{\theta}$ identifies the tumor cells from
287 the normal cells for both SU006 (Supplementary Fig. 11) and SU008, and clearly
288 delineates a subclone in SU008 marked by a copy-neutral LOH event on chr4a (Fig. 4c).
289 Focusing on SU008, we call the cell lineage that carries the chr4a LOH event clone-2,
290 and the other lineage clone-1. In parallel, clustering by peaks cleanly separates the tumor
291 cells from the epithelial cells and fibroblasts (Fig. 4d: left), and further, demarcates two
292 distinct clusters in the tumor cells (peaks-1 and peaks-2) (Fig. 4d: middle). What is the
293 relationship between the peaks-1 and peaks-2 clusters obtained from peak signals to the
294 two clones delineated by chr4a LOH? Coloring by chr4a major haplotype proportion ($\hat{\theta}$)
295 on the peaks-derived UMAP shows that the LOH in this region is carried by almost all of
296 the cells in peaks-2 but only a subset of the cells in peaks-1 (Fig. 4d: middle). This can
297 also be clearly seen in the density of $\hat{\theta}$ (Fig. 4d: right): While $\hat{\theta}$ is heavily concentrated
298 near 1 for peaks-2, it is bimodal for peaks-1. Since clone-1 and clone-2 are differentiated
299 by a copy-neutral event, this separation by peaks into two clusters is not driven by broad
300 differences in total copy number. Since clone-2 is split into two groups of distinct peak
301 signals, we infer that the chromatin remodeling underlying the divergence of the peaks-2
302 cells must have occurred in the clone-2 lineage, after the chr4a LOH event (Fig. 4e). In
303 this way, Alleloscope analysis of this scATAC-seq data set allowed us to overlay two
304 subpopulations defined by peak signals with two subpopulations defined by a subclonal
305 copy-neutral LOH, and infer their temporal order.

Figure 4.

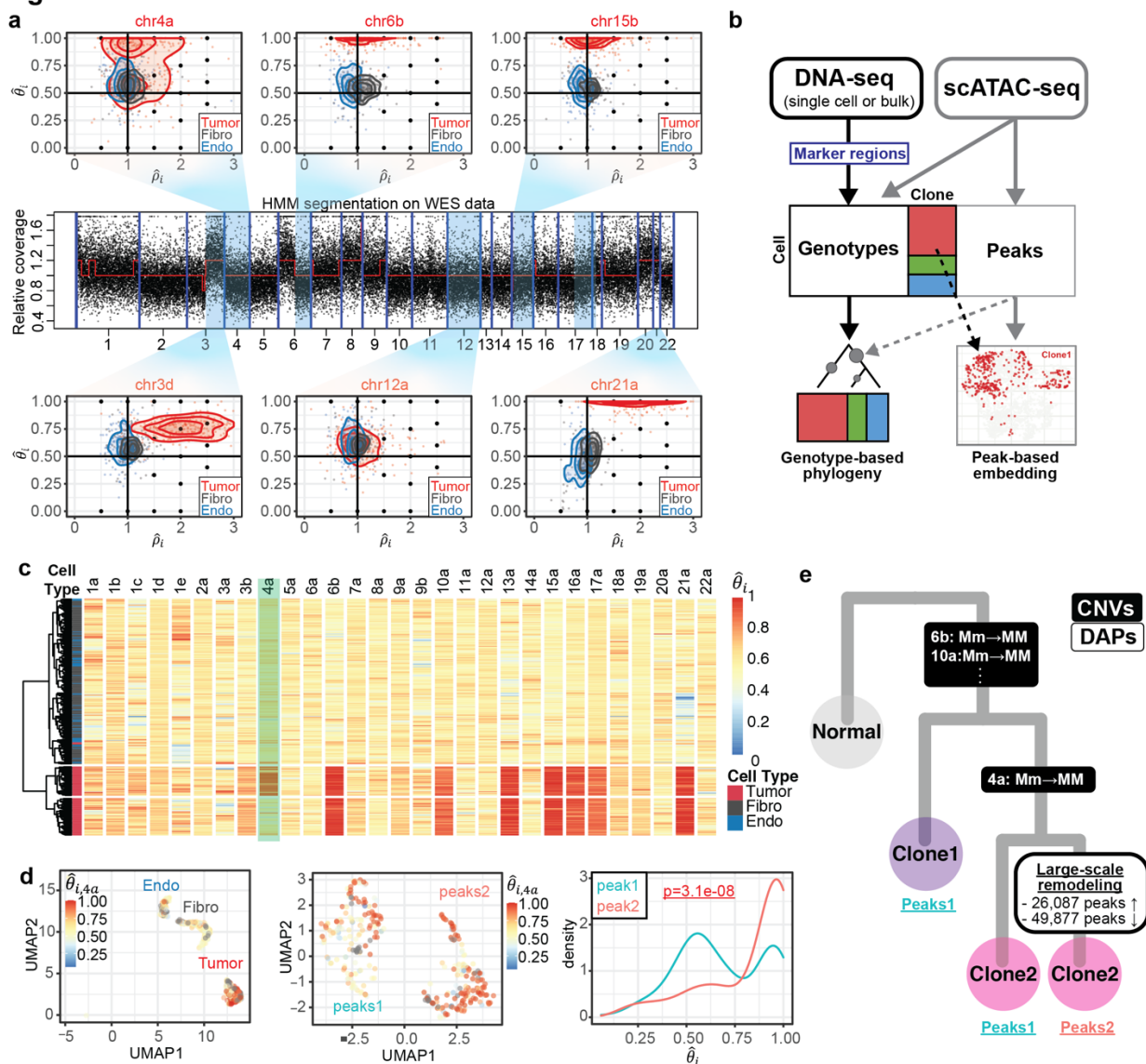


Fig. 4: Alleloscope multiomic analysis of scATAC-seq data of a basal cell carcinoma sample (SU008²³). (a) Genotype profiles for six example regions for cells in scATAC-seq data. The regions are taken from segmentation of matched whole exome sequencing (WES) data. Each dot represents a cell-specific ($\hat{\rho}_i, \hat{\theta}_i$) pair. Cells are colored by annotation derived from peak signals²³, Tumor: tumor cells, Fibro: fibroblasts, Endo: Endothelial cells]. Density contours are computed for each cell type (tumor, fibroblasts, endothelial) separately and shown by color on the plot. The lower-case letters following the chromosome number in the titles denote the ordered genomic segments. (b) Pipeline for multi-omics analysis integrating allele-specific copy number estimates and chromatin accessibility peak signals on ATAC-seq data. (c) Hierarchical clustering of cells by major haplotype proportion ($\hat{\theta}$) allows the separation of tumor cells from normal cells, as well as the differentiation of a subclone within the tumor cells. The marker region on chr4a separating the two tumor subclones is highlighted. (d) Integrated visualization of chr4a major haplotype proportion ($\hat{\theta}_i$) and genome-wide peak profile. Left: UMAP projection of the 788 cells in the dataset by their genome-wide peak profile, colored by $\hat{\theta}_i$. The cell type annotation (endothelial, fibroblasts, and tumor cells) is labeled in the plot. Middle: UMAP projection of only the 308 tumor cells by their genome-wide peak profile shows two well-separated clusters: peaks1 and peaks2. Right: Density of $\hat{\theta}_i$ values for the peaks1 and peaks2 subpopulations. (e) Intratumor

heterogeneity of SU008 is shaped by a subclonal LOH of chr4a followed by subsequent genome-wide chromatin remodeling leading to three subpopulations: Clone 1 which does not carry the chr4a LOH (peaks cluster 1), Clone 2 carrying the chr4a LOH (peaks cluster 1), and remodeled clone 2 (peaks cluster 2).

306

307 **Integrative analysis of clonal evolution and altered chromatin accessibility for a** 308 **complex polyclonal gastric cancer cell line**

309 The gastric cancer cell line SNU601 exhibits complex subclonal structure, as evidenced
310 by multiple multiallelic CNA regions (chr3e and chr18a are shown in Figure 3c). In addition
311 to scDNA-seq, we also performed scATAC-seq on this sample to profile the chromatin
312 accessibility of 3,515 cells at mean coverage of 73,845 fragments per cell. This allows us
313 to compare the allele-specific copy number profiles obtained by scATAC-seq with those
314 given by scDNA-seq and integrate the two data types in a multi-omic characterization of
315 this complex tumor.

316 First, we segmented the genome and estimated the allele-specific copy number profiles
317 of single cells at each segment for both the scATAC-seq and scDNA-seq data, following
318 the procedure in Figure 1 with some modifications due to the lack of normal cells to use
319 as control for this sample (see methods). Figure 5a shows the relative total coverage,
320 pooled across cells from scDNA-seq. Figure 5b shows $(\hat{\rho}, \hat{\theta})$ -scatterplots for five example
321 CNA regions in scDNA-seq and scATAC-seq. Compared to the scATAC-seq data, the
322 scDNA-seq data has about 8-fold higher total read coverage and 7-fold higher
323 heterozygous site coverage per cell. Thus, while subclones corresponding to distinct
324 haplotype profiles are cleanly separated in the scDNA-seq data, they are much more
325 diffuse in the scATAC-seq data. Yet, cluster positions in scATAC-seq roughly match those

326 in scDNA-seq. As expected, the $(\hat{\rho}, \hat{\theta})$ -scatterplots reveal the high level of chromosomal
327 instability in this sample, with each region exhibiting multiple clusters of different
328 haplotype structures that indicate the existence of subclones carrying mirrored events
329 and, for some regions, the variation of haplotype dosage over a gradient across cells.

330 Figure 5c shows the hierarchical clustering of cells from scDNA-seq based on their allele-
331 specific copy number profiles, revealing the subclonal structure and the co-segregating
332 CNA events that mark each subclone. For each cell in each region, Alleloscope also
333 produces a confidence score for its assignment to different haplotype profiles
334 (Supplementary Fig. 12). Based on visual examination of the confidence scores at the
335 marker regions, we identified 6 subclones for further investigation (Clones 1-6 labeled at
336 the right of the heatmap). The allele-specific copy number profiles allow us to manually
337 reconstruct the probable evolutionary tree relating these 6 clones under the following
338 three rules:

339 (1) Parsimony: The tree with the least number of copy number events is preferred.

340 (2) Monotonicity: For a multi-allelic region with escalating amplifications (e.g. Mm, MMm,
341 MMMm), the haplotype structures were produced in a monotonic order (e.g. Mm→
342 MMm→ MMMm) unless a genome doubling event occurred.

343 (3) Irreversibility of LOH: Once a cell completely loses an allele (i.e. copy number of that
344 allele becomes 0), it can no longer gain it back.

345 The evolutionary tree, thus derived, is shown in Figure 6b. The mirrored-subclonal
346 amplifications on chr3q, the deletion on chr4p, and the multiallelic amplification on chr20q

347 allowed us to infer the early separation of clones 3-6 from clones 1-2. Subclones 3-6 are
348 confidently delineated by further amplifications on chr3q, chr20q, chr11, chr13, and chr17.
349 Note that high chromosomal instability led to concurrent gains of 1q and 7p in both the
350 Clone 1-2 and Clone 3-6 lineages. We also observed a large number of low-frequency
351 but high-confidence CNA events indicating that ongoing chromosomal instability in this
352 population is spawning new sporadic subclones that have not had the chance to expand.

353 We now turn to scATAC-seq data, focusing on the 10 marker regions which, together,
354 distinguish Clones 1-6: chr1b, 3b-d, 4b, 7a, 11b, 13b, and 20b-c. The $(\hat{\rho}, \hat{\theta})$ values
355 computed by Alleloscope allows us to directly assign allele-specific copy number profiles
356 to each cell for each region, as well as subclone labels to each cell, with posterior
357 confidence score. The subclone assignment utilizes a Bayesian mixture model that pools
358 information across the 10 marker regions. Despite the low accuracy in per-region
359 genotyping, when information is pooled across the 10 marker regions, 81.6% of the 2,753
360 cells after filtering can be assigned to a subclone with >95% posterior confidence
361 (Supplementary Fig. 13, the number of ATAC cells confidently assigned to each clone
362 are shown in Figure 6a.). These subclone assignments for each cell, and cell-level
363 haplotype profiles for each region, can now be integrated with peak-level signals.

Figure 5.

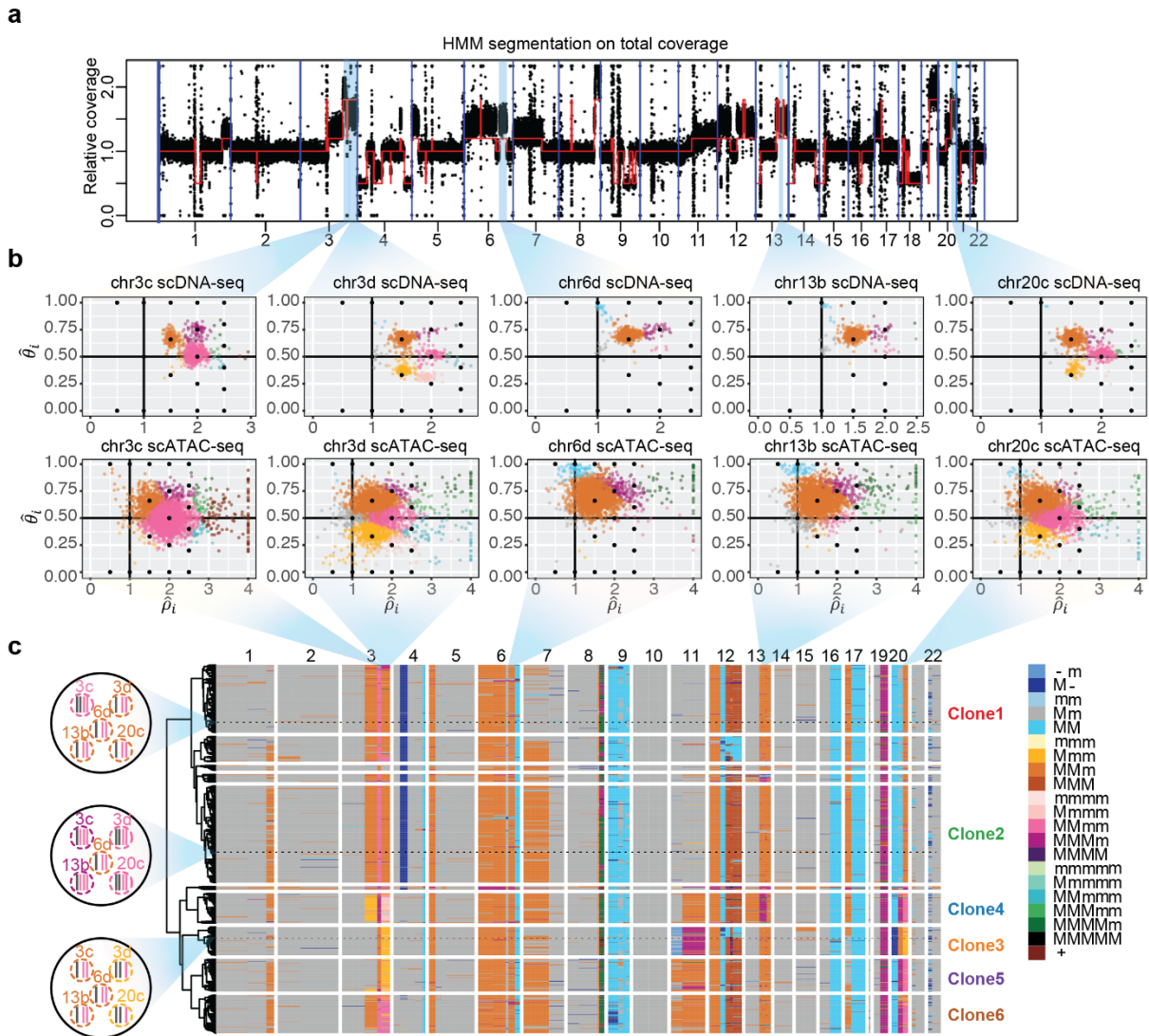


Fig. 5: Alleloscope analysis of scDNA-seq and scATAC-seq data reveals complex subclonal heterogeneity in the SNU601 gastric cancer cell line. (a) Genome segmentation using HMM on the pooled total coverage profile computed from scDNA-seq data.

(b) Single cell allele-specific copy number profiles ($\hat{\theta}$, $\hat{\rho}$) for five regions in scDNA-seq and scATAC-seq data. Cells are colored by haplotype profiles according to legend in Figure 5c.

(c) Tumor subclones revealed by hierarchical clustering of allele-specific copy number profiles from the scDNA-seq data. Genotypes of the five regions shown in Figure 5b, for three example cells, are shown in the left. The haplotype structures for the 5 regions in Figure 5b of three cells randomly chosen from Clone 1, 2, and 3, are shown to the left of the heatmap. In the color legend, M and m represent the “Major haplotype” and “minor haplotype” respectively. The six clones selected for downstream analysis in scATAC-seq data are labeled in the plot.

365 Following the scheme in Figure 4b, we computed the Uniform Manifold Approximation
366 and Projection (UMAP) coordinates for the scATAC-seq cells based on their peak profiles,
367 which gives a two-dimensional visualization of the geometry of the chromatin accessibility
368 landscape of this sample (Fig. 6a). UMAP scatterplots colored by clone assignment show
369 that the 6 clones exhibit marked differences in their chromatin accessibility profiles (Fig.
370 6a): While Clone 1 and Clone 2 are concentrated at the top half of the UMAP, Clones 3-
371 5 are positioned almost exclusively at the bottom half. Clone 6, which exhibits more
372 variance, is also significantly enriched at the bottom half of the UMAP. Among Clones 3-
373 5, Clone 3 has a distinct chromatin accessibility profile that is mostly concentrated at the
374 bottom tip, Clone 4 is positioned higher, while Clone 5 contains cells that are similar to
375 both clones 3 and 4. We expect some of these peak-level differences to be driven by
376 CNAs.

377 To delineate the peaks that differ between clones, and to distinguish peak differences
378 that are not accountable by CNAs, we identified differential accessibility peaks (DAPs)
379 across each split of the tree (Fig. 6b) by performing pairwise Chi-square tests for peak
380 enrichment between the cell populations on the two branches. The DAPs are categorized
381 into two groups —1. DAPs lying in CNA regions for which the direction of change aligns
382 with the direction of change of DNA coverage, and 2. DAPs not in CNA regions and DAPs
383 in CNA regions that don't align in directionality of change with DNA coverage. The number
384 of DAPs in both groups are shown along each branch (Fig. 6b). For the smaller subclones
385 (Clone 3,4,5), low coverage limits the detection power and thus limits the DAP counts in
386 both categories. Yet, juxtaposing DAP and CNA events along the tumor phylogeny yields
387 insights: Along most lineages, a significant proportion of DAPs are attributable to CNAs

388 (p-values shown along each branch), and CNA events drive a substantial 36.3% of all of
389 the DAPs identified. This argues for the importance of CNAs as a mechanism underlying
390 subclonal differences in chromatin accessibility in this tumor.

391 Nevertheless, along some branches we find a large number of DAPs not attributable to
392 broad CNAs, and thus must be due to other mechanisms. Two example DAPs of this
393 latter category are shown as insets in Figure 6b, with full list given in Supplementary Table
394 1. The first example is a peak at the transcription start site (TSS) of the REC8 gene, which
395 is located on chr14 where no apparent CNAs were observed across the six major
396 subclones. The TSS of REC8 is open in clones 3-6 but closed in clones 1-2 (p-
397 value<0.0001). REC8 is a gene encoding a meiosis-specific cohesion component that is
398 normally suppressed in mitotic proliferation, and its role in cancer has recently gained
399 increasing attention and controversy: While Yu et al.³⁸ found the expression of this gene
400 to suppress tumorigenicity in a gastric cancer cell line, McFarlane et al.³⁹ postulated that
401 it may be broadly activated in some cancers where it generates LOH by reductional
402 segregation. The opening of the TSS of REC8, stably maintained in Clones 3-6, suggests
403 that meiotic processes may underlie the increased chromosomal instability of this
404 multiclonal lineage. The second example is a peak at the TSS of the WWOX gene, located
405 on chr16, which is significantly depleted in Clone 3 (p-value<0.0001). Although chr16 has
406 LOH across all tumor cells, there are no detectable subclonal differences, and thus we
407 don't expect the decrease in accessibility at WWOX for subclone 3 to be due to a large
408 copy number event. Since WWOX is a well-known tumor suppressor whose down-
409 regulation is associated with more advanced tumors^{40, 41}, its decrease in accessibility
410 suggests a more aggressive phenotype for Clone 3. Overall, these two examples show

- 411 how Alleloscope can be used to dissect the roles of CNA and chromatin-level changes in
- 412 the identification of gene targets for follow-up study.

414 **Discussion**

415 Despite the recent advances in the application of single cell sequencing to cancer, we are
416 still far from understanding the diversity of genomes that are undergoing selection at the
417 single cell level. Notably, little is yet known about the intratumor diversity of allelic
418 configurations within CNV regions, and to what extent the diversity of cells in chromatin
419 accessibility can be attributed to diversity in allele-specific copy number. We presented
420 Alleloscope, a new method for allele-specific copy number estimation that can be applied
421 to single cell DNA and ATAC sequencing data (separately or in combination). First, on
422 scDNA-seq data of 9 samples from 3 different tumor types, with phasing validation by
423 linked-read sequencing on three samples, Alleloscope revealed an unprecedented level
424 of allelic heterogeneity within hypermutable CNA regions. In these regions, subclones
425 reside on a gradient of allelic ratios that is unobservable in total copy number analysis. In
426 simple cases, these hypermutable regions contain mirrored subclones, as previously
427 identified^{9,10}, but are often much more complex. We observed multiple instances of
428 recurrent CNA events, some verified by linked read sequencing, where the same region
429 is mutated multiple times during the evolution of the tumor, arriving at the same haplotype
430 profile in distinct clones. In accordance with the findings in Watkins et al.⁴², we found
431 using Alleloscope that chromosomal instability drives the formation of subclones not only
432 in primary tumors but also after metastasis.

433 Having established the allelic complexity of CNAs at single cell resolution, we next applied
434 Alleloscope to scATAC-seq data, thus enabling the combined study of clonal evolution
435 and chromatin accessibility. First, we considered the analysis of a public data set
436 consisting of two basal cell carcinoma samples, for which matched bulk whole-exome

437 sequencing data was used for initial genome segmentation upon which single cell CNA
438 genotyping was then conducted in the scATAC-seq data. Here we showed that
439 Alleloscope can detect amplifications, deletions, and copy-neutral LOH events accurately
440 in scATAC-seq data, and was able to find a subclone delineated by a copy-neutral LOH
441 event. Juxtaposing this subclone assignment with peak signals allowed us to detect a
442 wave of genome-wide chromatin remodeling in the lineage carrying the LOH. Next, we
443 applied Alleloscope to a complex polyclonal gastric cancer cell line with matched scDNA-
444 seq data. We found, by overlaying peak signals with subclones delineated by allele-
445 specific copy number estimates, that much of the intratumor heterogeneity in chromatin
446 accessibility can be attributed to CNAs. Focusing on subclone-enriched peaks outside of
447 CNA regions allowed the prioritization of genes for downstream follow-up.

448 Alleloscope can potentially be applied to the integration of single cell data of other
449 modalities, for example scATAC-seq and scRNA-seq data, to investigate the relationships
450 between clonal evolution, chromatin remodeling, and transcriptome. To facilitate
451 experimental design for single cell omics sequencing protocols, we investigated the
452 performance of Alleloscope under different scenarios (number of cells, total per cell
453 coverage, and total coverage at heterozygous SNP sites), see Supplementary Methods.
454 As expected, accuracy is a function of all three quantities (Supplementary Fig. 14).
455 Coverage at heterozygous SNP sites is especially important for scRNA-seq and scATAC-
456 seq data, for which shifts in total coverage is an unreliable proxy for underlying DNA copy
457 number. For scATAC-seq, the lower heterozygosity within peak regions led to lower
458 number of reads mapping to heterozygous loci as compared to scDNA-seq, and this
459 resulted in noisier subclone detection. Most of the current scRNA-seq technologies only

460 sequence either the 3' or 5' end of the mRNA transcripts, which limits the number of
461 heterozygous SNP sites covered by reads. The latest developments in single cell long
462 read sequencing⁴³⁻⁴⁵ and single cell multimodal sequencing⁴⁶ herald new analysis
463 opportunities with this method.

464 **Methods**

465 ScDNA-seq Data Sets and Pre-processing

466 Table 1 summaries the nine 10x scDNA-seq samples analyzed in this study:

Sample	Cancer type	Source	Paired normal	Linked -reads	Coverage per cell	Cell number	Ref
P5846	Gastric	Primary tissue	Yes	No	454,806	510	33
P5847	Gastric	Primary tissue	Yes	No	422,134	715	33
P5915	Colorectal	Liver meta	Yes	No	126,2629	233	33
P5931	Gastric	Primary tissue	Yes	Yes	730,932	796	12
P6198	Colorectal	Liver meta	Yes	Yes	532,343	2,271	33
P6335	Colorectal	Omentum meta	No	Yes	564,058	953	33
P6461	Colorectal	Liver meta	Yes	No	483,524	1,242	33
SNU601	Gastric	Ascites meta	No	No	565,648	1,531	12
BC10x	Breast	Primary tissue	No	No	781,506	1,916	10

467 The Cell Ranger DNA pipeline ([https://support.10xgenomics.com/single-cell-](https://support.10xgenomics.com/single-cell-dna/software/)
468 [dna/software/](https://support.10xgenomics.com/single-cell-dna/software/)) automates sample demultiplexing, read alignment, CNA calling and
469 visualization. We first applied the tool to process the sequencing data (beta version:
470 6002.16.0) using the GRCh38 reference genome. The output bam files from the tool
471 contain all information for later analysis. If the tumor samples had a matched normal
472 sample, the GATK HaplotypeCaller was used to reliably call heterozygous SNPs on the
473 matched normal samples. Otherwise, SNPs were retrieved on the tumor sample
474 themselves. Next, we applied VarTriX, a software tool for extracting single cell variant
475 information from the 10x barcoded bam files (<https://github.com/10XGenomics/vartrix>), to

476 efficiently generate two SNP-by-cell matrices for both reference alleles and alternative
477 alleles of the SNPs called in the previous step.

478 To include high-quality SNPs in the later analysis, we filtered out the SNPs with <5 reads
479 for P5846 and P5847, <10 reads for P5915 and P5931, <15 reads for P6335 and P6461,
480 <20 reads for P6198 and SNU601, and <40 for BC10X samples based on the number of
481 SNP detected for each sample. Additionally, SNPs located in the regions of repetitive
482 sequences such as centromeres and telomeres were excluded. To exclude cells that
483 might undergo apoptosis or cell cycles, the cells labeled noisy from the metadata output
484 by the Cell Ranger tool were excluded.

485 Single-cell ATAC Data sets, Sequencing and Preprocessing

486 Table 2 summaries the scATAC-seq samples analyzed in this study:

Sample	Cancer type	Source	Matched DNA	Coverage per cell	Cell number	Ref
SU006	Basal cell carcinoma	Primary tissue	Yes	41,368	2771	23
SU008	Basal cell carcinoma	Primary tissue	Yes	36,057	788	23
SNU601	Gastric	Ascites meta	Yes	73,845	3614	-

487

488 The scATAC-seq dataset for the SNU601 sample was generated in this study. About
489 400,000 cells were washed with RPMI media and centrifuged (400g for 5 min at 4°C)
490 twice. The supernatant was removed and chilled PBS + 0.04% BSA solution was added.
491 The resuspended pellet was added to a 2ml microcentrifuge tube and centrifuged (400g
492 for 5min at 4°C). After removing the supernatant without disrupting the pellet, 100 µL of
493 chilled Lysis Buffer (10 mM Tris-HCl (pH 7.4), 10 mM NaCl, 3 mM MgCl₂, 1% BSA, 0.1%

494 Nonidet P40 Substitute, 0.1% Tween-20 and 0.01% digitonin) was added and carefully
495 mixed 10 times. The tube was incubated on ice for 7 min. After incubation, 1 mL of chilled
496 Wash Buffer (10 mM Tris-HCl (pH 7.4), 10 mM NaCl, 3 mM MgCl₂, 1% BSA and 0.1%
497 Tween-20) was added and mixed 5 times followed by centrifugation of nuclei (500g for 5
498 min at 4°C). After removing the supernatant carefully, nuclei were resuspended in chilled
499 Nuclei Buffer (10X Genomics), filtered by Flowmi Cell Strainer (40µM) and counted using
500 a Countess II FL Automated Cell Counter. Then the nuclei were immediately used to
501 generate scATAC-seq library.

502 ScATAC-seq library was generated using the Chromium Single Cell ATAC Library & Gel
503 Bead Kit (10X Genomics) following the manufacturer's protocol. We targeted 3000 nuclei
504 with 12 PCR cycles for sample index PCR. Library was checked by 2% E-gel
505 (Thermofisher Scientific) and quantified using Qubit (Thermofisher Scientific).
506 Sequencing was performed on Illumina NextSeq500 using NextSeq 500/550 High Output
507 Kit v2.5 (Illumina).

508 Raw sequencing reads of the SNU601 scATAC-seq sample was de-multiplexed with the
509 10x Genomics Cell Ranger ATAC Software (v.1.2.0; [https://support.10xgenomics.com/single-](https://support.10xgenomics.com/single-cell-atac/software/pipelines/latest/algorithms/overview)
510 [cell-atac/software/pipelines/latest/algorithms/overview](https://support.10xgenomics.com/single-cell-atac/software/pipelines/latest/algorithms/overview)) and aligned to the human GRCh38
511 reference genome. The aligned scATAC-seq data of the two pre-treatment basal cell
512 carcinoma samples (SU006 and SU008) were downloaded from the Gene Expression
513 Omnibus under accession GSE129785²³. To obtain all potential SNPs for the SU006 and
514 SU008 samples, GATK Mutect2 was used to call all single-nucleotide variants (SNVs) on
515 the deduplicated bam files by the Picard toolkits of both the t-cell dataset and the tumor
516 dataset from the same tumor. All SNVs from the paired tumor-normal datasets were

517 combined and the read counts of these SNPs were quantified for each cell in the tumor
518 scATAC-seq dataset. The pre-filtered cell barcodes for the two public scATAC-seq
519 datasets were retrieved from the previous study²³. For the SNU601 scATAC-seq data, we
520 instead quantified the read counts of the two alleles of the SNPs more reliably called from
521 the paired normal scDNA-seq data. Like scDNA-seq, we applied VarTrix to generate two
522 SNP-by-cell matrices for both reference alleles and alternative alleles of all the SNVs for
523 all the scATAC-seq datasets. To obtain a SNP set including only SNVs that are more
524 possible to be germline SNPs, we further filtered out the SNVs <20 reads for the SU008
525 sample and <30 reads for the SU006 sample. SNPs with extreme VAF values <0.1 or
526 >0.9 were also excluded for both samples. Since we used the phasing information from
527 the paired scDNA-seq data to assist the estimation of the haplotype structures for the
528 SNU601 scATAC-seq data, we instead filtered out the cells <5 reads and the SNPs <5
529 reads to improve quality of the downstream analysis.

530 *Linked-reads sequencing and data processing*

531 The three samples with the linked-reads sequencing data were acquired as surgical
532 resections following informed consent under an approved institutional review board
533 protocol from Stanford University. Samples were subjected to mechanical and enzymatic
534 dissociation as previously described, followed by cryopreservation of dissociated cells³³.
535 Cryofrozen cells were rapidly thawed in a bead bath at 37 °C. Cell counts were obtained
536 on a BioRad TC20 cell counter (Biorad, Hercules, CA) using 1:1 trypan blue dilution.
537 Between 1.5-2.5 million total cells were washed twice in PBS. Centrifugation was carried
538 out at 400g for 5 minutes. PBS was removed and cell pellets were frozen at -80 °C. DNA

539 extraction was carried out on cell pellets following thawing using either MagAttract HMW
540 DNA Kit (P5931) or AllPrep DNA/RNA Mini Kit (Qiagen Inc., Germantown, MD, USA) as
541 per manufacturer's protocol. Quantification was carried out using Qubit (ThermoFisher
542 Scientific).

543 Sequencing libraries were prepared from DNA using Chromium Genome Reagent Kit (v2
544 Chemistry) (10X Genomics, Pleasanton, CA, USA) as per manufacturer's instructions.
545 Sequencing was performed using Illumina HiSeq or NovaSeq sequencers using 150x150
546 bp paired end sequencing and i7 index read of 8 bp. Long Ranger (10X Genomics)
547 version 2.2.0 was used to perform read alignment to GRCh38, calling and phasing of
548 SNPs, indels and structural variants.

549 Segmentation

550 The first step of Alleloscope is to segment the genome into regions with different CNA
551 profiles. The appropriate segmentation algorithm depends on what samples are available.
552 First, matched bulk DNA sequencing data (WGS/WES) or pseudo-bulk data from
553 scDNAseq data can be segmented using FACLON⁵, a segmentation method that jointly
554 models the bulk coverage and bulk VAF profiles, if a matched normal sample is available.
555 To accommodate segments from rare subclones, methods that integrate shared cellular
556 breakpoints in CNA detection for scDNA-seq data such as SCOPE⁴⁷ can improve
557 sensitivity. Since FALCON requires a matched normal sample or a sufficiently large set
558 of normal cells, if these are not available then Alleloscope instead relies on an HMM-
559 based segmentation method. The HMM method, which operates on the binned counts of
560 pooled cells, assumes a Markov transition matrix on four hidden states representing

561 deletion, copy-neutral state, single-copy amplification and double-copy amplification:

562
$$\begin{pmatrix} 1-3t & t & t & t \\ t & 1-3t & t & t \\ t & t & 1-3t & t \\ t & t & t & 1-3t \end{pmatrix},$$
 where $t = 1 \times 10^{-6}$ as default. Emission probabilities

563 follow a normal distribution with means equal to {1.8, 1.2, 1, 0.5} and standard deviations

564 equals to 0.2. All the scDNA-seq samples were segmented using the HMM algorithm.

565 With the paired sample, the P6198 tumor sample was segmented using FALCON on the

566 1,399,650 SNPs >30 reads across 2,271 cells with all the default parameters.

567 Whole-exome sequencing (WES) data processing

568 The WES data of the two paired tumor-normal samples (SU006 and SU008) were

569 obtained from the Sequence Read Archive under accession PRJNA533341. Raw fastq

570 files were aligned to the GRCh37 reference genome using bwa-mem⁴⁸ with duplicate

571 reads removed using the Picard toolkits⁴⁹. The copy number calls of paired normal-tumor

572 samples were obtained using VarScan²⁵⁰. To perform allele-specific copy number

573 analysis on the WES using FALCON, GATK HaplotypeCaller⁴⁹ was used to call SNPs on

574 both tumor and normal samples. Then FALCON was used to segment each chromosome

575 based on the read counts of the reference alleles and alternative alleles of the SNPs

576 overlapped between the paired tumor-normal samples.

577 SNP Phasing and Single-cell Allele Profile Estimation

578 For each region after segmentation, an expectation-maximization (EM)- based method is

579 used to iteratively phase each SNP and estimate cell-specific allele-specific copy number

580 states for all scDNA-seq and scATAC-seq data sets. Recall that by “major haplotype” we

581 refer to the haplotype with higher aggregate copy number in the sample. Let I_j indicate
 582 whether the reference allele of SNP j is located on the major haplotype and θ_i denote
 583 major haplotype proportion of cell i . The EM model iterates the expectation step and the
 584 maximization step. The complete log likelihood of the model is

$$585 \quad l(\theta) = \sum_{j=1}^n \log P(A_{ij}, B_{ij} | \theta)$$

$$586 \quad = \sum_{j=1}^n \{ [A_{ij} \log \theta + B_{ij} \log(1 - \theta)] I_j + [B_{ij} \log \theta + A_{ij} \log(1 - \theta)] (1 - I_j) \}$$

587 where A_{ij} and B_{ij} are the observed read counts for the reference and alternative alleles
 588 of cell i on SNP j . In the E-step, we first calculate the expected value of the posterior
 589 probability of the hidden variable I_j to construct a lower bound for optimization

$$590 \quad E_{\hat{\theta}_i^{(t)}} [I_j | A_{ij}, B_{ij}] = \hat{I}_j^{(t)} = \frac{\prod_i \hat{\theta}_i^{(t) A_{ij}} (1 - \hat{\theta}_i^{(t)})^{B_{ij}}}{\prod_i \hat{\theta}_i^{(t) A_{ij}} (1 - \hat{\theta}_i^{(t)})^{B_{ij}} + \prod_i (1 - \hat{\theta}_i^{(t)})^{A_{ij}} \hat{\theta}_i^{(t) B_{ij}}}$$

591 where $\hat{\theta}_i^{(t)}$ is the parameter from the t^{th} iteration. In the M-step, $\hat{\theta}_i$ is updated by solving

$$592 \quad \hat{\theta}_i^{(t+1)} = \operatorname{argmax}_{\theta_i} E [l(\theta) | A_{ij}, B_{ij}, \hat{\theta}_i^{(t)}]$$

$$593 \quad = \frac{\sum_j [A_{ij} \hat{I}_j^{(t)} + B_{ij} (1 - \hat{I}_j^{(t)})]}{\sum_j [A_{ij} \hat{I}_j^{(t)} + B_{ij} (1 - \hat{I}_j^{(t)})] + \sum_j [A_{ij} (1 - \hat{I}_j^{(t)}) + B_{ij} \hat{I}_j^{(t)}}$$

594 Where $\hat{\theta}_i^{(t)}$ and $\hat{\theta}_i^{(t+1)}$ are from two successive iterations of EM. The two steps are
 595 iterated until converge. To speed up the EM process, we limited the maximum number of

596 SNPs in a region to be 30,000 in our analysis. For the SNU601 scATAC-seq dataset,
597 since the phase were estimated in the paired scDNA-seq dataset with higher depth, we
598 directly applied the estimated \hat{l}_j 's from scDNA-seq data to estimate the $\hat{\theta}_i$'s of the cells in
599 the scATAC-seq data. To improve the estimation results, cells with <20 read counts
600 covering the identified SNPs were excluded for each region.

601 *Selecting normal cells and normal regions for single-cell Coverage Normalization*

602 Let r represent a region in the genome after segmentation. To compute the relative
603 coverage change for each cell in region r ($\hat{\rho}_{ir}$), normal cells and diploid regions identified
604 within the sample are required for normalization. After major haplotype proportions for
605 each cell in each region $\hat{\theta}_{ir}$'s are inferred from the EM-based algorithm, the estimates are
606 used to identify normal cells and diploid regions under a hierarchical clustering of all cells.
607 To identify normal cells, the dendrogram tree is first cut into k largest groups (we used
608 $k = 5$ which worked well across samples). The cluster with normal cells is identified by
609 selecting the c^{th} cluster with the minimum distance calculated by

610
$$\sum_{r=1}^R \left| \frac{\sum_{\theta_i \in S_c} \hat{\theta}_{ir}}{n_c} - 0.5 \right|^2$$

611 where S_c represents $\hat{\theta}_i$ values of the cells in the c^{th} cluster, and n_c is total cell number in
612 the c^{th} cluster. All cells in the c^{th} cluster are considered as candidate normal cells.

613 Putative diploid regions are next identified in each cluster. Similar to normal cell
614 identification, Alleloscope computes the first measurement (d_{cr}) as the sum $\hat{\theta}_i$ distance
615 of the cells in the c^{th} cluster for each region r

616
$$d_{cr} = \sum_{\hat{\theta}_i \in S_c} |\hat{\theta}_{ir} - 0.5|^2$$

617 Since amplified regions with both haplotypes equally amplified can also have small sum
618 $\hat{\theta}_i$ distance, adjusted raw coverages are also considered in diploid region selection. The
619 adjusted raw coverage of cell i in region r ($\tilde{\rho}_{ir}$) is computed by

620
$$\tilde{\rho}_{ir} = \frac{N_{ir}}{N_i} \times \frac{L_r}{LL}$$

621 where N_{ir} is the total read counts in region r of cell i and N_i is the total read counts of cell
622 i across the regions. L_r is length of the region r and LL is total length of the genome. For
623 region r , cells with $\tilde{\rho}_{ir}$ values larger than the 99th percentile are assigned the $\tilde{\rho}_{ir}$ values
624 equal to the 99th percentile across the cells. The second measurement (m_{cr}) used to
625 select diploid regions in the c^{th} cluster is the mean $\tilde{\rho}_{ir}$ for each region r

626
$$m_{cr} = \frac{\sum_i \tilde{\rho}_{ir} \tilde{\rho}_{ir}}{n_c}$$

627 where S_c here represents $\tilde{\rho}_i$ values of the cells in the c^{th} cluster. To identify diploid regions,
628 d_{cr} and m_{cr} are both ranked from the smallest to the largest for each cluster c .
629 Alleloscope shows a list of potential diploid regions for each cluster by raking the sums
630 of d_{cr} ranks and m_{cr} ranks. Excluding the c^{th} cluster identified as the normal group,
631 Alleloscope proposed a list for the candidate diploid regions across the clusters by
632 selecting the majority region.

633 Since coverage on scATAC-seq data is confounded by the epigenetic signals,
634 chromosome 22 for SU008 and chromosome 18 for SU006 were directly selected as

635 normal regions based on the WES data. Individual cells were classified into normal and
636 tumor cells based on the epigenetic signals on the scATAC-seq data. For the SNU601
637 scATAC-seq dataset, chromosome 10 was selected as the normal region based on the
638 paired scDNA-seq data.

639 Cell-level Genotyping

640 The cell-level allele-specific copy number profiles are defined by both relative coverage
641 change ($\hat{\rho}_{ir}$) and major haplotype proportion ($\hat{\theta}_{ir}$) of region r and cell i. After the normal
642 cells and normal control region are identified, cell-specific relative coverage change in
643 region r is calculated as

$$644 \quad \hat{\rho}_{ir} = \frac{N_{ir}}{N_{i0}} / \text{median}\left(\frac{N_{0r}}{N_{00}}\right)$$

645 where N_{ir} is total read counts in region r and N_{i0} is total read counts in a reference region
646 of cell i. N_{0r} is a vector denoting total read counts in region r of all identified normal cells
647 and N_{00} is a vector denoting total read counts in the same reference region r of all
648 identified normal cells. Since SNU601 is a tumor cell line with no normal cells in the
649 dataset, N_{0r} and N_{00} were calculated from the cells in the matched normal P6198 sample
650 as a substitute for the scDNA-seq data. For SNU601 scATAC-seq data, we aligned the
651 distribution of the $\hat{\rho}_{ir}$ values in paired scDNA-seq data to the distribution of the $\frac{N_{ir}}{N_i}$ values
652 for each region to get the normalized $\hat{\rho}_{ir}$ in the scATAC-seq data. The normalized $\hat{\rho}_{ir}$
653 values for the scATAC-seq data were computed by

$$654 \quad \hat{\rho}_{ir}^{atac} = \frac{N_{ir}}{N_{i0}} / \text{median}\left(\frac{N_{ir}}{N_{i0}}\right) \times \text{median}(\hat{\rho}_{ir}^{dna})$$

655 Next, cells with extreme $\hat{\rho}_{ir}$ values larger than the 99th percentile and smaller than the
656 first percentile across the cells are considered outliers and excluded for each region. With
657 the $(\hat{\rho}_{ir}, \hat{\theta}_{ir})$ pairs, cells in the scDNA-seq data can be classified into the haplotype profiles
658 (g) with the expected (ρ_g, θ_g) values based on minimum distance. Although signals in the
659 scATAC-seq data are much noisier, the haplotype structures identified in the paired
660 scDNA-seq data can help to guide the genotyping for each region. In region r, the
661 posterior probability of cell i carrying a haplotype profile observed in region r in the paired
662 scDNA-seq data was

$$663 \quad P(GT_{ir} = g_r | \hat{\rho}_{ir}, \hat{\theta}_{ir}) = \frac{P(\hat{\rho}_{ir}, \hat{\theta}_{ir} | GT_{ir} = g_r) \pi_{g_r}}{\sum_{g_r'} P(\hat{\rho}_{ir}, \hat{\theta}_{ir} | GT_{ir} = g_r') \pi_{g_r'}}$$

664 where g_r denotes the haplotype profiles observed in region r in the paired scDNA-seq
665 data and π_{g_r} denotes the prior probability that a randomly sampled cell carrying the g_r
666 haplotype profile. A uniform prior can be used for π_{g_r} in the absence of external
667 information. In the formula,

$$668 \quad P(\hat{\rho}_{ir}, \hat{\theta}_{ir} | GT_{ir} = g_r) = P(\hat{\rho}_{ir} | \mu = \rho_g; \sigma_\rho = 0.25) \times P\left(\hat{\theta}_{ir} \middle| \mu = \theta_g; \sigma = \sqrt{\frac{\hat{\theta}_{ir}(1 - \hat{\theta}_{ir})}{n_{ir}}}\right),$$

669 where n_{ir} is the number of total read counts in region r for cell i. The haplotype profile of
670 cell i in region r was estimated by maximizing the above posterior probability. The
671 haplotype profiles of each region are visualized using different colors in the two-
672 dimensional scatter plots for both scDNA-seq and scATAC-seq data with the confidence

673 scores calculated using the distance of the points to the canonical centers and the
674 standard deviations.

675 Validations using paired linked-reads sequencing data

676 We validated our algorithm using paired linked-reads sequencing data with two strategies
677 in one gastric cancer patient sample and two colorectal cancer patient samples. First, the
678 phasing accuracy was assessed by comparing the estimated SNP phases on the scDNA-
679 seq data and the known phases of the same SNPs from the linked-reads sequencing data
680 in individual regions. In the linked-reads sequencing data, SNPs within the same phase
681 sets are phased with respect to one another, while those between different SNP sets are
682 not. Therefore, we compared the phases of the SNPs overlapping between our estimated
683 SNP set and the phase set with the largest numbers of SNPs in the linked-reads
684 sequencing data for each region. The reference alleles of the overlapping SNPs with \hat{I}_j
685 >0.5 are estimated to be on the major haplotype. Otherwise, the reference alleles of the
686 overlapping SNPs with $\hat{I}_j <0.5$ are estimated to be on the minor haplotype. The SNPs with
687 $\hat{I}_j=0.5$ are excluded. By comparing estimated phases and known phases from the linked-
688 reads sequencing data of the overlapping SNPs, the phasing accuracy was computed for
689 each region.

690 Secondly, we evaluated the genotyping accuracy by comparing the estimated haplotype
691 profiles of each cell and the haplotype profiles inferred from the linked-reads sequencing
692 data in individual regions. In the linked-reads sequencing data, the phase set with the
693 largest numbers of SNPs was selected. The known phases of the overlapping SNPs
694 between the phase set and the estimated SNPs were used to infer θ_i for each cell. Cell-

695 level haplotype profiles using θ_i 's from linked-reads sequencing data were considered as
696 gold standard. By comparing the estimated haplotype profiles from $\hat{\theta}_i$ and the haplotype
697 profiles from θ_i , genotyping accuracy was computed for each region. If the number of
698 overlapping SNPs for an amplified region is smaller than 5000, the phase sets were
699 combined from the largest to the smallest to reduce variance of θ_i 's inferred from linked-
700 reads sequencing data. The estimated SNP phases (\hat{I}_j) were used as templates to
701 combine separate phase sets.

702 Cell Lineage Reconstruction

703 To investigate the tumor subclonal structure for scDNA-seq data, cell-specific haplotype
704 profiles from Alleloscope across the genome were used to reconstruct cell lineage trees.
705 The “Gower’s distance” is calculated using “cluster” R package on the nominal haplotype
706 profiles between cells. Then hierarchical clustering is performed on the distance using the
707 “ward.D2” method. Since variance of $\hat{\theta}_i$'s is higher when fewer SNPs are located in a
708 segment, we included the segments with more than 2,000 SNPs identified. The clustering
709 results are visualized using the ‘pheatmap’ R package. Each segment was plotted with
710 its length proportional to 5,000,000 bins. The heights of the clustering tree were log-
711 transformed for easier visualization.

712 The tumor subclonal structures were also investigated in the scATAC-seq data. Instead
713 of using the haplotype profiles defined by the $(\hat{\rho}_{ir}, \hat{\theta}_{ir})$ pairs, the cells from the two public
714 basal cell carcinoma were clustered using $\hat{\theta}_{ir}$ values, which are orthogonal to the peak
715 signals based on total coverage, across the segments with more than 500 SNPs. Then
716 hierarchical clustering is performed on the Euclidean distance using the “ward.D2”

717 method and visualized using ‘pheatmap’ R package with the three largest clusters
718 separated by marginal lines. The heights of the clustering tree were log-transformed for
719 easier visualization.

720 Since the subclones for the SNU601 sample were identified first from the scDNA-seq data,
721 for this cell we adopted a supervised strategy to assign each cell into different subclones.
722 First, we identified 10 marker regions-- chr1b, 3b-d, 4b, 7a, 11b, 13b, and 20b-c that help
723 to differentiate the cells into the six major subclones based on the subclone specific copy
724 number profiles from the scDNA-seq data. Combining the haplotype profiles across the
725 ten regions for each cell enables assignment of the cells into one of the six subclones
726 with high confidence. The posterior probability of cell i coming from clone k was

$$727 \quad P(\text{Clone}_i = k | \hat{\rho}_i, \hat{\theta}_i) = \frac{P(\hat{\rho}_i, \hat{\theta}_i | \text{Clone}_i = k) \pi_k}{\sum_{k'} P(\hat{\rho}_i, \hat{\theta}_i | \text{Clone}_i = k') \pi_{k'}}$$

728 where $k \in \{1 \sim 6\}$ for the six clones and π_k is the prior probability that a randomly sampled
729 cell coming from the k^{th} clone, which can be estimated from the paired scDNA-seq data
730 or set to uniform (in our analysis setting to uniform gives very similar results). In the
731 formula,

$$732 \quad P(\hat{\rho}_i, \hat{\theta}_i | \text{Clone}_i = k) = \prod_x P(\hat{\theta}_{ix}, \hat{\rho}_{ix} | \text{Clone}_i = k)$$
$$733 \quad = \prod_x \phi\left(\frac{\hat{\theta}_{ix} - \theta_{kx}}{\sqrt{n_{ix} \theta_{kx} (1 - \theta_{kx})}}\right) \phi\left(\frac{\hat{\rho}_{ix} - \rho_{kx}}{\sigma_\rho}\right),$$

734 where x is the index for the ten marker regions, $\hat{\theta}_{ix}$ and $\hat{\rho}_{ix}$ are the estimated major
735 haplotype proportion and relative coverage for cell i in the scATAC-seq data, θ_{kx} and ρ_{kx}

736 are the “known values” for specific haplotype profiles for clone k derived from the paired
737 scDNA-seq data, and n_{ix} is the number of total read counts in the x^{th} marker region for
738 cell i. Each cell was assigned into one of the six subclones by maximizing the above
739 posterior probability with the confidence score being the posterior probability of the
740 assigned clone.

741 ScATAC-seq data analysis

742 To investigate the relationships between allele-specific CNAs and chromatin accessibility,
743 for each cell in scATAC-seq data we processed the peak signals in addition to the allele-
744 specific CNAs. For the two public basal cell carcinoma samples, the peak by cell matrices
745 was obtained from GSE129785. We subset the fragment counts for each peak in the cells
746 from the SU008 sample, regressed out cell total coverage for each peak by linear
747 regression, and projected the cells onto the UMAP plot using genome-wide peak signals⁵¹.
748 The cell type identify for each cluster was retrieved from the labels in the previous study²³.
749 To further explore intratumor heterogeneity, we selected the cells labeled as tumor cells,
750 regressed out cell total coverage, and projected the tumor cells onto the UMAP plot like
751 previously described. Then the DNA level information and epigenetic signals for each cell
752 can be visualize and analyzed together.

753 For the SNU601 scATAC-seq dataset, scATAC-pro⁵² was used to call peaks and
754 generate the peak by cell matrix from the bam file and fragment file output by the Cell
755 Ranger software. We first filtered out the cells that have proportions of fragments on the
756 detected peaks <0.4 and or total peaks outside of the range 15,000~100,000, and filtered
757 out the peaks observed in less than 0.1 of cells. Next, we regressed out cell total coverage

758 for each peak by linear regression, and projected the cells onto the UMAP plot using
759 genome-wide peak signals. Then the clonal assignment based on the DNA information
760 and the peak signals can be integrated at the single-cell level.

761 Based on the lineage structure from the paired scDNA-seq data, the cells can also be
762 placed in the lineage tree based on their clonal assignment. Under the lineage structure,
763 pairwise comparison using Chi-squared test was performed on the proportion of the to
764 identify differential accessible peaks (DAPs) for each branch. A peak was considered a
765 DAP if the FDR adjusted p-values<0.05. Since copy number alterations are confounding
766 factors that also affect the peak signals, the DAPs were further divided into two groups—
767 1. “CNA” group if the DAPs are in the CNA regions and both signals are positive correlated;
768 2. “Other” group if the DAPs are not categorized in the first group. A set of DAPs were
769 considered to be enriched in the CNA regions if the p-values<0.05 under the
770 hypergeometric test. This type of analysis enables investigation of the relationships
771 between the two signals. Each DAP was further mapped to the genes that are potentially
772 regulated based on the $\pm 2,000$ bp distance on the genome. To further visualize the
773 difference of the peak signals among the six clones, the peak signals were pooled across
774 the cells and normalized by the total cell number in each subclone.

775 **Data availability**

776 All the linked-reads sequencing data and the scATAC-seq dataset are available under
777 accession ###. There are no restrictions on data availability or use. The patient scDNA-
778 seq data were obtained from dbGAP under accession phs001818.v3.p1³³ (all except
779 5931 scDNA) and phs001711¹² (5931 scDNA). The cell line scDNA-seq dataset was from

780 the Sequence Read Archive (SRA) under accession PRJNA498809. The public scATAC-
781 seq data and whole exome sequencing data were obtained from the SRA under
782 accession PRJNA532774²³ and PRJNA533341³⁷.

783 **Code availability**

784 Alleloscope is available on GitHub at <https://github.com/seasoncloud/Alleloscope>.

785 **Reference**

- 786 1. Baylin, S.B. & Jones, P.A. A decade of exploring the cancer epigenome - biological
787 and translational implications. *Nat Rev Cancer* **11**, 726-734 (2011).
- 788 2. Sandoval, J. & Esteller, M. Cancer epigenomics: beyond genomics. *Curr Opin*
789 *Genet Dev* **22**, 50-55 (2012).
- 790 3. Greaves, M. & Maley, C.C. Clonal evolution in cancer. *Nature* **481**, 306-313 (2012).
- 791 4. Burrell, R.A., McGranahan, N., Bartek, J. & Swanton, C. The causes and
792 consequences of genetic heterogeneity in cancer evolution. *Nature* **501**, 338-345
793 (2013).
- 794 5. Chen, H., Bell, J.M., Zavala, N.A., Ji, H.P. & Zhang, N.R. Allele-specific copy
795 number profiling by next-generation DNA sequencing. *Nucleic Acids Res* **43**, e23
796 (2015).
- 797 6. Favero, F. et al. Sequenza: allele-specific copy number and mutation profiles from
798 tumor sequencing data. *Ann Oncol* **26**, 64-70 (2015).
- 799 7. Ha, G. et al. TITAN: inference of copy number architectures in clonal cell
800 populations from tumor whole-genome sequence data. *Genome Res* **24**, 1881-
801 1893 (2014).

- 802 8. Shen, R. & Seshan, V.E. FACETS: allele-specific copy number and clonal
803 heterogeneity analysis tool for high-throughput DNA sequencing. *Nucleic Acids*
804 *Res* **44**, e131 (2016).
- 805 9. Jamal-Hanjani, M. et al. Tracking the Evolution of Non-Small-Cell Lung Cancer. *N*
806 *Engl J Med* **376**, 2109-2121 (2017).
- 807 10. Zaccaria, S. & Raphael, B.J. Characterizing allele- and haplotype-specific copy
808 numbers in single cells with CHISEL. *Nat Biotechnol* (2020).
- 809 11. Van Loo, P. et al. Allele-specific copy number analysis of tumors. *Proc Natl Acad*
810 *Sci U S A* **107**, 16910-16915 (2010).
- 811 12. Andor, N. et al. Joint single cell DNA-seq and RNA-seq of gastric cancer cell lines
812 reveals rules of in vitro evolution. *NAR Genom Bioinform* **2**, lqaa016 (2020).
- 813 13. Bakker, B. et al. Single-cell sequencing reveals karyotype heterogeneity in murine
814 and human malignancies. *Genome Biol* **17**, 115 (2016).
- 815 14. Garvin, T. et al. Interactive analysis and assessment of single-cell copy-number
816 variations. *Nat Methods* **12**, 1058-1060 (2015).
- 817 15. Kim, C. et al. Chemoresistance Evolution in Triple-Negative Breast Cancer
818 Delineated by Single-Cell Sequencing. *Cell* **173**, 879-893 e813 (2018).
- 819 16. Laks, E. et al. Clonal Decomposition and DNA Replication States Defined by
820 Scaled Single-Cell Genome Sequencing. *Cell* **179**, 1207-1221 e1222 (2019).
- 821 17. Navin, N. et al. Tumour evolution inferred by single-cell sequencing. *Nature* **472**,
822 90-94 (2011).
- 823 18. Velazquez-Villarreal, E.I. et al. Single-cell sequencing of genomic DNA resolves
824 sub-clonal heterogeneity in a melanoma cell line. *Commun Biol* **3**, 318 (2020).

- 825 19. Wang, Y. et al. Clonal evolution in breast cancer revealed by single nucleus
826 genome sequencing. *Nature* **512**, 155-160 (2014).
- 827 20. Corces, M.R. et al. The chromatin accessibility landscape of primary human
828 cancers. *Science* **362** (2018).
- 829 21. Granja, J.M. et al. Single-cell multiomic analysis identifies regulatory programs in
830 mixed-phenotype acute leukemia. *Nat Biotechnol* **37**, 1458-1465 (2019).
- 831 22. Litzénburger, U.M. et al. Single-cell epigenomic variability reveals functional
832 cancer heterogeneity. *Genome Biol* **18**, 15 (2017).
- 833 23. Satpathy, A.T. et al. Massively parallel single-cell chromatin landscapes of human
834 immune cell development and intratumoral T cell exhaustion. *Nat Biotechnol* **37**,
835 925-936 (2019).
- 836 24. Schep, A.N., Wu, B., Buenrostro, J.D. & Greenleaf, W.J. chromVAR: inferring
837 transcription-factor-associated accessibility from single-cell epigenomic data. *Nat*
838 *Methods* **14**, 975-978 (2017).
- 839 25. Cabal-Hierro, L. et al. Chromatin accessibility promotes hematopoietic and
840 leukemia stem cell activity. *Nat Commun* **11**, 1406 (2020).
- 841 26. Dravis, C. et al. Epigenetic and Transcriptomic Profiling of Mammary Gland
842 Development and Tumor Models Disclose Regulators of Cell State Plasticity.
843 *Cancer Cell* **34**, 466-482 e466 (2018).
- 844 27. Guilhamon, P. et al. Single-cell chromatin accessibility in glioblastoma delineates
845 cancer stem cell heterogeneity predictive of survival. *bioRxiv*, 370726 (2020).
- 846 28. Pan, D. et al. A major chromatin regulator determines resistance of tumor cells to
847 T cell-mediated killing. *Science* **359**, 770-775 (2018).

- 848 29. Qu, K. et al. Chromatin Accessibility Landscape of Cutaneous T Cell Lymphoma
849 and Dynamic Response to HDAC Inhibitors. *Cancer Cell* **32**, 27-41 e24 (2017).
- 850 30. Shaffer, S.M. et al. Rare cell variability and drug-induced reprogramming as a
851 mode of cancer drug resistance. *Nature* **546**, 431-435 (2017).
- 852 31. Shu, S. et al. Synthetic Lethal and Resistance Interactions with BET Bromodomain
853 Inhibitors in Triple-Negative Breast Cancer. *Mol Cell* **78**, 1096-1113 e1098 (2020).
- 854 32. Tirosh, I. et al. Dissecting the multicellular ecosystem of metastatic melanoma by
855 single-cell RNA-seq. *Science* **352**, 189-196 (2016).
- 856 33. Sathe, A. et al. The cellular genomic diversity, regulatory states and networking of
857 the metastatic colorectal cancer microenvironment. *bioRxiv* (2020).
- 858 34. Bell, J.M. et al. Chromosome-scale mega-haplotypes enable digital karyotyping of
859 cancer aneuploidy. *Nucleic Acids Res* **45**, e162 (2017).
- 860 35. Greer, S.U. et al. Linked read sequencing resolves complex genomic
861 rearrangements in gastric cancer metastases. *Genome Med* **9**, 57 (2017).
- 862 36. Zheng, G.X. et al. Haplotyping germline and cancer genomes with high-throughput
863 linked-read sequencing. *Nat Biotechnol* **34**, 303-311 (2016).
- 864 37. Yost, K.E. et al. Clonal replacement of tumor-specific T cells following PD-1
865 blockade. *Nat Med* **25**, 1251-1259 (2019).
- 866 38. Yu, J. et al. REC8 functions as a tumor suppressor and is epigenetically
867 downregulated in gastric cancer, especially in EBV-positive subtype. *Oncogene* **36**,
868 182-193 (2017).
- 869 39. McFarlane, R.J. & Wakeman, J.A. Meiosis-like Functions in Oncogenesis: A New
870 View of Cancer. *Cancer Res* **77**, 5712-5716 (2017).

- 871 40. Aqeilan, R.I. et al. Loss of WWOX expression in gastric carcinoma. *Clin Cancer*
872 *Res* **10**, 3053-3058 (2004).
- 873 41. Barylá, I., Styczen-Binkowska, E. & Bednarek, A.K. Alteration of WWOX in human
874 cancer: a clinical view. *Exp Biol Med (Maywood)* **240**, 305-314 (2015).
- 875 42. Watkins, T.B.K. et al. Pervasive chromosomal instability and karyotype order in
876 tumour evolution. *Nature* (2020).
- 877 43. Gupta, I. et al. Single-cell isoform RNA sequencing characterizes isoforms in
878 thousands of cerebellar cells. *Nat Biotechnol* (2018).
- 879 44. Lebrigand, K., Magnone, V., Barbry, P. & Waldmann, R. High throughput error
880 corrected Nanopore single cell transcriptome sequencing. *Nat Commun* **11**, 4025
881 (2020).
- 882 45. Singh, M. et al. High-throughput targeted long-read single cell sequencing reveals
883 the clonal and transcriptional landscape of lymphocytes. *Nat Commun* **10**, 3120
884 (2019).
- 885 46. Zhu, C., Preissl, S. & Ren, B. Single-cell multimodal omics: the power of many.
886 *Nat Methods* **17**, 11-14 (2020).
- 887 47. Wang, R., Lin, D.Y. & Jiang, Y. SCOPE: A Normalization and Copy-Number
888 Estimation Method for Single-Cell DNA Sequencing. *Cell Syst* **10**, 445-452 e446
889 (2020).
- 890 48. Li, H. & Durbin, R. Fast and accurate short read alignment with Burrows-Wheeler
891 transform. *Bioinformatics* **25**, 1754-1760 (2009).

- 892 49. McKenna, A. et al. The Genome Analysis Toolkit: a MapReduce framework for
893 analyzing next-generation DNA sequencing data. *Genome Res* **20**, 1297-1303
894 (2010).
- 895 50. Koboldt, D.C. et al. VarScan 2: somatic mutation and copy number alteration
896 discovery in cancer by exome sequencing. *Genome Res* **22**, 568-576 (2012).
- 897 51. McInnes, L., Healy, J. & Melville, J. Umap: Uniform manifold approximation and
898 projection for dimension reduction. *arXiv preprint arXiv:1802.03426* (2018).
- 899 52. Yu, W., Uzun, Y., Zhu, Q., Chen, C. & Tan, K. scATAC-pro: a comprehensive
900 workbench for single-cell chromatin accessibility sequencing data. *Genome Biol*
901 **21**, 94 (2020).

902 **Acknowledgements**

903 The work is supported by the National Institutes of Health [P01HG00205ESH to B.T.L.,
904 S.M.G. AND H.P.J., 5R01-HG006137-07 and 1U2CCA233285-01 to C.-Y.W. and to
905 N.R.Z.]. Additional support to HPJ came from the Research Scholar Grant, RSG-13-297-
906 01-TBG from the American Cancer Society, Clayville Foundation and the Gastric Cancer
907 Foundation.

908 **Author contributions**

909 C.-Y.W. and N.R.Z. conceived the computational methods and designed the study with
910 help from H.P.J. C.-Y.W. developed and implemented the computational methods and
911 conducted all data analyses. B.T.L. helped in data interpretation. B.T.L., H.K. and A.S.
912 performed all related sample preparation and sequencing. S.M.G. performed data pre-
913 processing and coordinated data transfer. H.P.J. advised all experiments and data

914 collection. C.-Y.W., N.R.Z, and H.P.J. wrote the manuscript. All authors read and
915 approved the final manuscript.

916 **Competing interests**

917 The authors declare no competing interests.